Heliyon 9 (2023) e18297

Contents lists available at ScienceDirect

Heliyon

journal homepage: www.cell.com/heliyon

Research article

Deep learning-based label-free hematology analysis framework using optical diffraction tomography

Dongmin Ryu [a,1], Taeyoung Bak [b,1], Daewoong Ahn [a], Hayoung Kang [a], Sanggeun Oh [a], Hyun-seok Min [a], Sumin Lee [a,*], Jimin Lee [c,d,**]

[a] Tomocube Inc., Daejeon, 34109, Republic of Korea
[b] Department of Computer Science and Engineering, Ulsan National Institute of Science and Technology (UNIST), Ulsan, 44919, Republic of Korea
[c] Department of Nuclear Engineering, Ulsan National Institute of Science and Technology (UNIST), Ulsan, 44919, Republic of Korea
[d] Graduate School of Artificial Intelligence (AIGS), Ulsan National Institute of Science and Technology (UNIST), Ulsan, 44919, Republic of Korea

ARTICLE INFO

Keywords:
Label-free imaging
Optical diffraction tomography
Hematology analysis
Deep learning
Object detection

ABSTRACT

Hematology analysis, a common clinical test for screening various diseases, has conventionally required a chemical staining process that is time-consuming and labor-intensive. To reduce the costs of chemical staining, label-free imaging can be utilized in hematology analysis. In this work, we exploit optical diffraction tomography and the fully convolutional one-stage object detector or FCOS, a deep learning architecture for object detection, to develop a label-free hematology analysis framework. Detected cells are classified into four groups: red blood cell, abnormal red blood cell, platelet, and white blood cell. In the results, the trained object detection model showed superior detection performance for blood cells in refractive index tomograms (0.977 mAP) and also showed high accuracy in the four-class classification of blood cells (0.9708 weighted F1 score, 0.9712 total accuracy). For further verification, mean corpuscular volume (MCV) and mean corpuscular hemoglobin (MCH) were compared with values obtained from reference hematology equipment, with our results showing reasonable correlation in both MCV (0.905) and MCH (0.889). This study provides a successful demonstration of the proposed framework in detecting and classifying blood cells using optical diffraction tomography for label-free hematology analysis.

1. Introduction

Hematology analysis is one of the most common clinical tests used to look for various disorders such as sepsis [1–3], infection [4–6], anemia [7–9], and blood cancer [10–13]. Chemical staining has traditionally been used for blood analysis, with requirements for complex equipment, numerous chemical reagents, difficult system calibration and procedures, and highly skilled personnel, factors that can significantly impact the status of cells during the process [14,15]. Additionally, the staining process itself is time-consuming and difficult; it is generally estimated that it takes approximately 45 min for specialists to stain cells in accordance with strict staining protocols and to assess the staining quality under a microscope [15].

* Corresponding author at: Tomocube Inc., Daejeon, 34109, Republic of Korea.
** Corresponding author at: Department of Nuclear Engineering, Ulsan National Institute of Science and Technology (UNIST), Ulsan, 44919, Republic of Korea.
E-mail addresses: slee@tomocube.com (S. Lee), jiminlee@unist.ac.kr (J. Lee).
[1] These authors contributed equally to this work.

https://doi.org/10.1016/j.heliyon.2023.e18297
Received 4 March 2023; Received in revised form 12 July 2023; Accepted 13 July 2023

Available online 20 July 2023

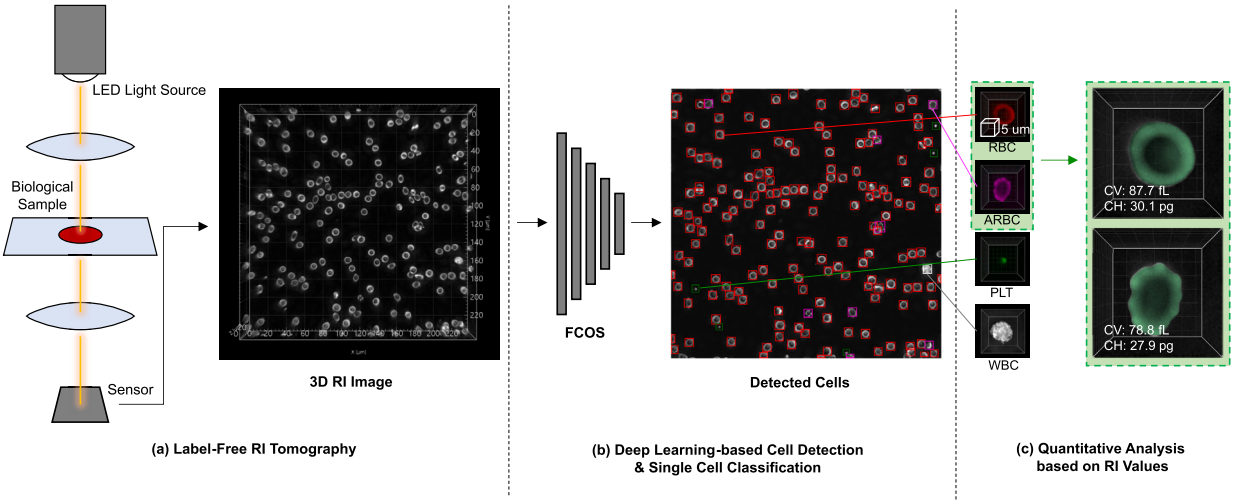

Fig. 1. Schematic diagram of hematological analysis using ODT. (a) A 3D RI tomogram of a blood sample is acquired by partially coherent ODT. (b) The deep learning model automatically detects blood cells and classifies them into four types: RBC, ARBC, PLT, and WBC. See Section 2.2 for a detailed explanation of the object detection model implementation. (c) For RBCs and ARBCs, morphological and biochemical quantities such as MCV and MCH are measured by their RI distribution.

To solve this problem, various methods using label-free imaging modalities in hematology analysis have been studied. For instance, Raman microscopy [16–18], hyperspectral imaging [19–21], and defocusing phase-contrast imaging [22,23] have been exploited for hematology analysis. These methods use the endogenous imaging contrast of samples themselves without using any staining agent, but require complex optical systems and long data acquisition times. Recently, investigations have adopted quantitative phase imaging (QPI) to enable reasonably quick and simple label-free imaging of biological samples [24,25]. The morphological and biochemical characteristics of a cell can be observed concurrently using QPI by measuring the phase delay of light passing through the sample and reconstructing the refractive index (RI) of the sample through the relationship between the scattered light and the sample.

Recent rapid advances in artificial intelligence (AI) have led to the application of AI to the QPI of various types of biological samples in a wide range of tasks including classification [26–30], segmentation [31–33], and inference [34–36]. In the field of blood cell identification, QPI and AI demonstrate a good synergy since they can simultaneously check morphological and biological properties in addition to their label-free nature and uniform data quality that is not affected by staining quality [37,28,29].

In this study, we utilize optical diffraction tomography (ODT) [38], a label-free and three-dimensional (3D) QPI modality that measures the RI distribution of a sample, and a deep learning technology for the hematological analysis of blood samples. Details of each step can be found in Fig. 1. To develop an object detection model for blood cells, the fully convolutional one-stage object detector (FCOS) [39], an anchor-free multitask deep learning model, is implemented and trained. With this framework, detected cells are classified into four groups: red blood cell (RBC), abnormal red blood cell (ARBC), platelet (PLT), and white blood cell (WBC). We demonstrate that the trained model is able to detect most of the cells, showing high accuracy in the four-class classification of blood cells. In addition, morphological and biochemical quantities are calculated, namely mean corpuscular volume (MCV) and mean corpuscular hemoglobin (MCH), for RBC and ARBC groups based on their RI distributions. Our quantitative analysis results also show highly acceptable agreement with commercial hematology analysis equipment.

2. Materials and methods

2.1. Dataset preparation

A total of 171 blood samples were collected from Chungnam National University Hospital (CNUH, Republic of Korea), and ODT was exploited to obtain RI tomograms of the blood samples. (This study was approved by the institutional review board at CNUH.) For each blood sample, 27 measurements were carried out because single-measurement coverage was restricted to 234 μm × 234 μm due to field-of-view limitations. Each measured 3D RI tomogram had a lateral resolution of 0.162 μm/pixel and axial resolution of 0.731 μm/pixel.

Bounding boxes and cell types for all blood cell instances were annotated for 1,224 3D RI tomograms by three experts. The blood cells were categorized into four types: RBC, ARBC meaning a morphologically irregular RBC, PLT, and WBC. The criteria for morphological irregularity was determined by annotators. A total of 115,143 cell instances were annotated to train and evaluate the object detection model (Table 1). The whole dataset was divided into a 7:2:1 ratio for training, validation, and testing.

Table 1
Distribution of cell types in the dataset.

Type of dataset	RBC	PLT	WBC	ARBC
Train	67,595	6,391	87	6,435
Validation	19,604	1,608	19	1,567
Test	9,661	1,143	18	1,015
Total	96,860	9,142	124	9,017

2.2. Training details of object detection models

In previous studies [40,41], YOLOv3 [42] or its variant model has been widely used and has shown reasonable performance. However, detection failures of PLTs were observed due to their small size compared to RBCs or WBCs. Hence, for the detection and identification of blood cells of various sizes, the FCOS, or fully connected one-stage object detector, [39], was exploited in this work, which is an anchor-free one-stage object detection framework optimized for detecting objects of various sizes at once.

For model implementation, the MMDetection library [43] was utilized, which is a PyTorch-based open-source object detection toolbox. FCOS detects objects by performing classification, regression, and centerness calculations on feature maps extracted from the backbone. In our experiments, we employed focal loss (FL, (1)), generalized intersection over union (GIoU, (2)) loss, and binary cross entropy (BCE, (3)) loss to evaluate classification, regression, and centerness prediction. These loss functions are the same as the improvement methods described in the original FCOS paper [39]. The mathematical formulations for these loss functions are defined as follows:

$$FL(p_t) = -\alpha_t(1-p_t)^{\gamma}\log(p_t), \tag{1}$$

$$GIoU = IoU(A,B) - \frac{|(C \backslash (A \cup B)|}{|C|}, \tag{2}$$

$$BCE = -[y\log(\hat{y}) + (1-y)\log(1-\hat{y})]. \tag{3}$$

In this paper, we applied all the enhancements presented in the work of Tian et al. [39] to the FCOS framework.

For preprocessing, min-max normalization was applied to the RI images. An augmentation ratio of 0.5 was applied to the training dataset using the horizontal flip operation. In the training phase, the batch size was set to 4. The AdamW optimizer was used, and the learning rate was applied as 0.0005. In addition, mixed precision and gradient clipping were applied, and the number of epochs was 30.

We tested three backbone networks for the FCOS framework, namely ResNet-18, ResNet-50, and the Swin Transformer, to find the architecture with the best performance [44,45]. Since ResNet, one of the most famous convolutional neural networks, is known as a good feature extractor in various vision tasks, two variants of ResNet were tested for the backbone of our network. Recently, backbones based on transformers [46] have also shown high performance in various vision tasks. First achieving state-of-the-art performance in object detection tasks in 2021 [45], the Swin Transformer has a characteristic that it performs self-attention only among patches within each window. Our data has the feature that similarly shaped and sized cells are evenly distributed throughout the entire image; thus, to investigate whether the features of the Swin Transformer's architecture can be advantageous for our images, we chose the Swin Transformer as one of the backbones. In the case of ResNet-18, the Feature Pyramid Networks (FPNs) to Path Aggregation Feature Pyramid Network (PAFPNs) were adjusted according to the model output, while for the Swin Transformer, the numbers of output channels and FPN input channels were adjusted.

Our network was implemented in PyTorch 1.12 using a graphics processing unit (GPU) server (Tesla V100 32GB). The GPU server environment was as follows: Python 3.8.12, CUDA 11.6, CUDNN 8.3.3, MMCV 1.5.1, and MMDetection 2.24.1.

2.3. Evaluation of the trained object detection model

A total of five metrics—mean average precision (mAP), recall (7), precision (8), F1 score (9), and total accuracy (10)—were calculated to evaluate the performance of the trained object detection model. In the case of mAP, the definition in the PASCAL VOC dataset was applied (average of 11-point interpolated AP, (4), (5), (6)). For an IoU threshold of 0.5, true and false cases were distinguished, and the average of the area under the precision-recall curve (PR curve) was used for each category. When calculating the base area, recall was divided into 0.1 units and interpolated with the highest precision value in the relevant section. Each metric is defined as follows:

$$AP = \frac{1}{11}\sum_{r\in(0.0,\ldots,1.0)} p_{interp}(r), \tag{4}$$

$$p_{interp}(r) = max_{\tilde{r}\geq r}p(\tilde{r}), \tag{5}$$

$$mAP = \frac{1}{N}\sum_{i=1}^{N} AP_i, \tag{6}$$

$$recall = \frac{TP}{TP+FN}, \tag{7}$$

Table 2
Comparison of the detection performance of each FCOS backbone.

Backbone	mAP	Number of model parameters
ResNet-18	0.970	**21.45** M
ResNet-50	0.970	32.12 M
Swin Transformer	**0.977**	35.56 M

$$precision = \frac{TP}{TP + FP}, \tag{8}$$

$$F1 = 2 \cdot \frac{precision * recall}{precision + recall}, \tag{9}$$

$$accuracy = \frac{TP + TN}{TP + FN + FP + TN}. \tag{10}$$

2.4. Comparison of blood cell indices

Refractive index, which is used as an imaging contrast in ODT, is a biochemical quantity related to the number of molecules per unit volume. With a 3D RI tomogram, RI can be used to calculate not only morphological quantities such as corpuscular volume (CV) but also biochemical quantities like corpuscular hemoglobin (CH). Therefore, hematological analysis using ODT opens the door to quantitative analysis beyond simple blood cell counting and classification. First, a cell contour is generated by a simple thresholding-based contouring algorithm. In this work, the threshold was set to 0.005, which means the cell contour was set based on the voxels where RI exceeds the medium RI + 0.005. Then CV is measured by equation (11).

$$CV = \#_{voxels} \times unitVolume, \tag{11}$$

where $\#_{voxels}$ denotes the number of voxels in a cell contour and $unitVolume$ is the volume of a single voxel, which is 0.0192 μm^3 for the device used in this study. CH is calculated as equation (12):

$$CH = (\mathrm{sum}(RI) - N \times n_m)/RII \times unitVolume, \tag{12}$$

where $\mathrm{sum}(RI)$ is the sum of RI values for all voxels in the cell contour, n_m denotes the RI of the medium (1.337 for water), and RII means refractive index increment [47–51], 0.0029 for this study.

By averaging the above quantities of each RBC instance in the same blood sample, the MCV and MCH of the blood sample are obtained. In this study, MCV and MCH were calculated for RBCs detected through the trained FCOS model for 1,539 3D RI tomograms, which were not included in the dataset for object detection model training and evaluation. The calculated values were compared with those measured from reference hematology analysis equipment (DxH-800 and LH-780, Beckman Coulter).

3. Results and discussion

3.1. Evaluation of the trained object detection model

The cell detection performance of each of the three backbones (ResNet-18, ResNet-50, and Swin Transformer) was first compared. Among the models used as the FCOS backbone, the Swin Transformer showed the best performance by a very narrow margin (Table 2). The highest performance was 0.977 mAP when the backbone network was the Swin Transformer, but it also had the largest number of model parameters, about 1.7 times that of ResNet-18. ResNet-18 and ResNet-50 showed similar performance.

The classification performance of the three backbone networks was also compared. ResNet-18 showed the highest classification performance with 0.9708 weighted F1 score and 0.9712 total accuracy. While the difference between these results and those from the Swin Transformer is relatively small (about 0.03), when compared to ResNet-50, ResNet-18 had higher scores of more than 0.1 (Table 3) Detailed classification results of each backbone network can be found in Fig. 2. Considering RBCs and ARBCs only, ResNet-18 failed 306 cases, while ResNet-50 and Swin Transformer failed 472 and 344 cases, respectively. Because of the severe data imbalance for the WBC class (only 124 cases in 115,143 cells), the WBC classification performance of each model was neglected.

In summary, ResNet-18 performed the best in terms of classification while achieving competitive detection performance despite having the smallest number of model parameters. Therefore, ResNet-18 was chosen to be utilized as the backbone of our hematology analysis framework.

Compared with the results of a previous related study [41], our model improved mAP by about 0.23, and the accuracy for the RBC, WBC, and PLT groups improved by more than 3%. Since our imaging modality is relatively new, it should be noted that there are no previous experimental results using the same type of modality.

Although our model achieved an F1 score over 0.8 for ARBC classification, it should be noted that the criteria for the ARBC/RBC boundary are ambiguous. Hence, there is a limit to determine the model's performance in identifying ARBCs through its accuracy with the label, since the standard of morphological irregularity for an ARBC depends on the annotator. To investigate ARBC classification performance in more detail, t-SNE [52] analysis, which is a method of reducing high-dimensional data to low-dimensional data, was performed using extracted features from the trained FCOS model. T-sne result can be found in Fig. 3 (a), and Fig. 3 (b) shows

Table 3
Comparison of the classification performance of each FCOS backbone.

Backbone	Class	Recall	Precision	F1 score	Weighted F1 score	Total Accuracy
ResNet-18	RBC	0.9873	0.9803	0.9838	**0.9708**	**0.9712**
	PLT	0.9912	0.9937	0.9925		
	WBC	0.9286	0.5417	0.6842		
	ARBC	0.7967	0.8645	0.8292		
ResNet-50	RBC	0.9596	0.9899	0.9745	0.9593	0.9568
	PLT	0.9924	0.9937	0.9930		
	WBC	0.8571	1.0000	0.9231		
	ARBC	0.9004	0.6871	0.7795		
Swin Transformer	RBC	0.9921	0.9716	0.9818	0.9663	0.9680
	PLT	0.9950	0.9901	0.9926		
	WBC	0.6875	1.0000	0.8148		
	ARBC	0.7090	0.8964	0.7918		

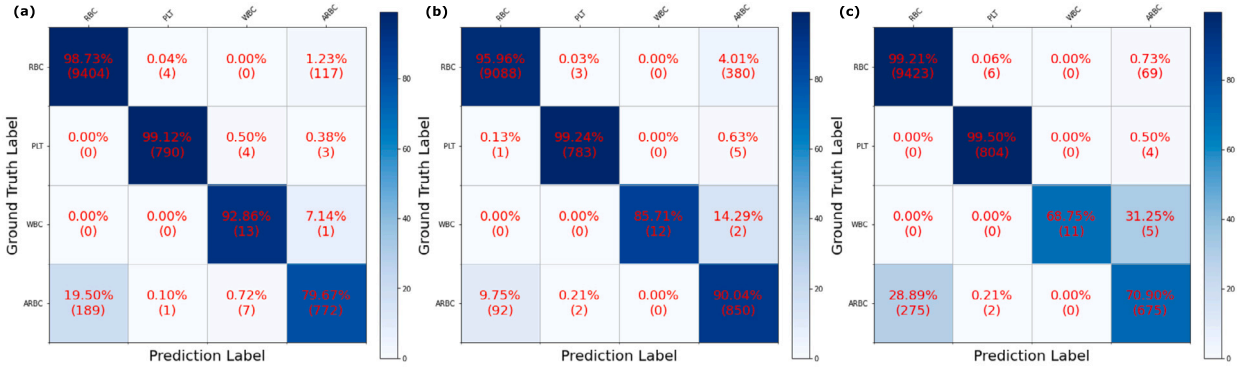

Fig. 2. Normalized confusion matrix results for each FCOS backbone: **(a)** ResNet-18, **(b)** ResNet-50, and **(c)** Swin Transformer. ResNet-18 showed the best performance in classifying RBCs and ARBCs.

representative sample RI images. For the feature extraction, cells detected in the RBC and ARBC channels were used, meaning that features were able to be extracted for both classes, as FCOS utilizes multiple binary classifiers for multi-class identification.

By projecting high-dimensional features extracted from the trained FCOS model onto a two-dimensional plane, we could see that the features were largely divided into two clusters with a gray area between them. As a result of visualizing numerous points corresponding to each prediction/label result shown in the figure legend, the morphological characteristics of a clear circular shape for RBCs and a clear irregular shape for ARBCs were observed at the ends, while cells of a shape difficult to assign to either class were observed in the middle area. These results demonstrate that our FCOS model distinguished RBCs and ARBCs based on their degree of morphological irregularity.

3.2. Comparison of blood cell indices

In terms of MCV and MCH, our results showed acceptable agreement with the reference equipment. Fig. 4 (a), (b) and (c) show MVC data comparison, and (d), (e), and (f) show MCH comparison. The Pearson correlation coefficients for MCV and MCH were 0.905 and 0.889, respectively, while the gradients of Passing–Bablok regression were 1.04 and 0.97, respectively.

The indices of the RBC and ARBC classes were also compared. Fig. 5 (a) shows cell indices comparison of MCV, and Fig. 5 (b) shows MCH results. There was a clear difference between the physical quantity distribution of RBCs and ARBCs. The MCV and MCH of the ARBCs were clearly lower than those of the RBCs. A larger divergence of the ARBC MCV and MCH was also observed, caused by the irregularity of the cell shape.

Discussion about the issue of cell contouring is required in this section. For an accurate quantitative analysis, an appropriate cell contour is necessary. Because of the low axial resolution caused by the missing cone problem [35], the RI distribution changes depending on the shape and angle of the cell. This causes distortion of the cell contour and consequently affects quantitative analysis. To solve this issue, recognition of the lying angle of each cell and corresponding compensation will be studied in follow-up research.

4. Conclusions

This study showed that the detection and classification of blood cells using ODT technology is feasible for label-free hematology analysis and also that physical quantities can be calculated with QPI equipment that uses refractive index as the imaging contrast. We applied FCOS, an anchor-free one-stage detection framework, for hematological analysis in 3D RI tomograms of blood samples. Our

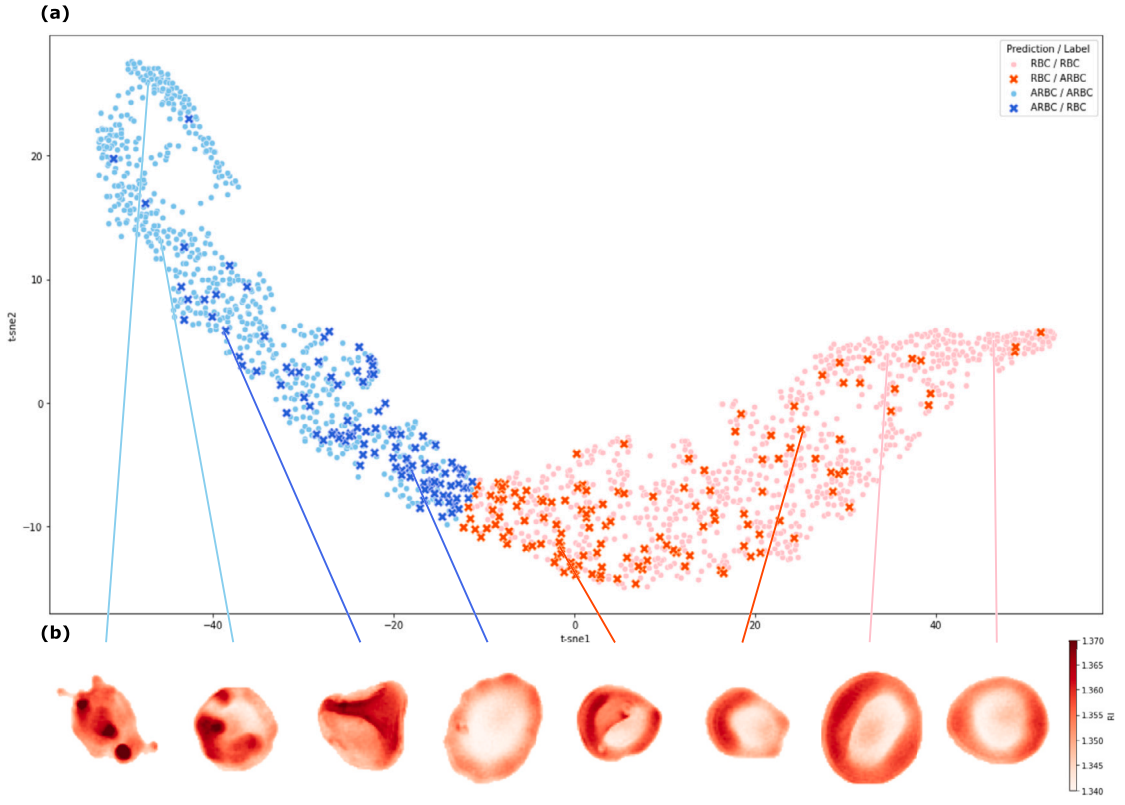

Fig. 3. t-SNE result of the classification model: **(a)** t-SNE plot and **(b)** representative sample RI images for each legend entry.

model achieved 0.977 mAP for blood cell detection, and achieved 0.9708 weighted F1 score and 0.9712 total accuracy for four-class blood cell classification (RBC, ARBC, PLT, and WBC). The RBC indices from the RI distribution in each cell were also calculated and compared with those obtained from reference equipment. The result showed reasonable correlation in MCV (0.905) and MCH (0.889) with the reference equipment.

While previous study [29] has conducted hematological analysis on single red blood cells (RBCs) using 3D QPI, the significance of our research lies in detecting blood cells and calculating the physical quantity of blood cells from the same type of blood sample used in actual clinical settings. Our proposed framework has high potential to be extended to more various types of hematology analysis, such as WBC subtype classification, through additional data acquisition.

Ethics approval statement

This study was approved by the institutional review board at Chungnam National University Hospital, Republic of Korea. (CNUH 2020-110914) As a retrospective study, waiver of informed consent was approved.

Funding

This work was supported in part by a grant of the Korea Health Technology R&D Project through the Korea Health Industry Development Institute (KHIDI), funded by the Ministry of Health and Welfare, Republic of Korea (HI21C1161), in part by an Institute of Information and communications Technology Planning and Evaluation (IITP) grant funded by the Ministry of Science and ICT (MSIT), Republic of Korea (No.2020-0-01336, Artificial Intelligence Graduate School Program (UNIST)), and in part by a grant of the National Research Foundation of Korea (NRF) funded by the MSIT, Republic of Korea (NRF-2021R1F1A1057818).

CRediT authorship contribution statement

Dongmin Ryu; Taeyoung Bak: Performed the experiments; Analyzed and interpreted the data; Wrote the paper.
Daewoong Ahn: Analyzed and interpreted the data.
Hayoung Kang; Sanggeun Oh: Contributed reagents, materials, analysis tools or data.
Hyun-seok Min: Conceived and designed the experiments; Analyzed and interpreted the data.
Sumin Lee; Jimin Lee: Conceived and designed the experiments; Analyzed and interpreted the data; Contributed reagents, materials, analysis tools or data; Wrote the paper.

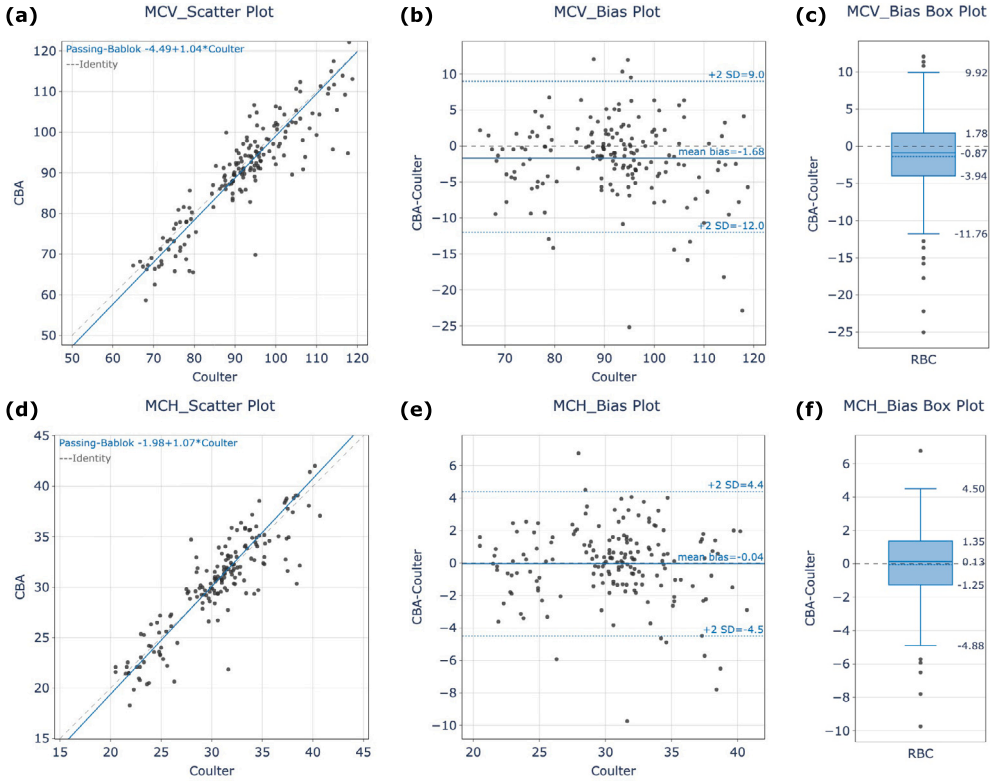

Fig. 4. Comparison of RBC indices, **(a–c)** MCV and **(d–f)** MCH, obtained from our model and the reference device. CBA denotes our result, and Coulter means the reference device.

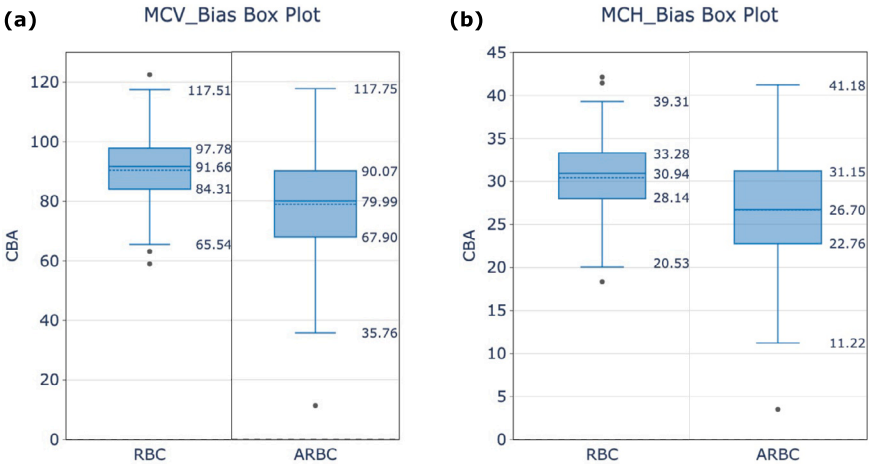

Fig. 5. Comparison of cell indices, **(a)** MCV and **(b)** MCH, for RBC and ARBC classes.

Declaration of competing interest

Dongmin Ryu, Daewoong Ahn, Hayoung Kang, Sangguen Oh, Hyun-seok Min, and Sumin Lee have financial interests in Tomocube Inc., a company that commercializes optical diffraction tomography and quantitative phase imaging instruments. The other authors declare no competing financial interests.

Data availability

The authors do not have permission to share data.

References

[1] K. Murphy, J. Weiner, Use of leukocyte counts in evaluation of early-onset neonatal sepsis, Pediatr. Infect. Dis. J. 31 (1) (2012) 16–19.
[2] R. Chandramohanadas, Y. Park, L. Lui, A. Li, D. Quinn, K. Liew, M. Diez-Silva, Y. Sung, M. Dao, C.T. Lim, et al., Biophysics of malarial parasite exit from infected erythrocytes, PLoS ONE 6 (6) (2011) e20869.
[3] O.K. Baskurt, D. Gelmont, H.J. Meiselman, Red blood cell deformability in sepsis, Am. J. Respir. Crit. Care Med. 157 (2) (1998) 421–427.
[4] M.H. Klinger, W. Jelkmann, Role of blood platelets in infection and inflammation, J. Interferon Cytokine Res. 22 (9) (2002) 913–922.
[5] L.A. Al-Gwaiz, H.H. Babay, The diagnostic value of absolute neutrophil count, band count and morphologic changes of neutrophils in predicting bacterial infections, Med. Princ. Pract. 16 (5) (2007) 344–347.
[6] T. Honda, T. Uehara, G. Matsumoto, S. Arai, M. Sugano, Neutrophil left shift and white blood cell count as markers of bacterial infection, Clin. Chim. Acta 457 (2016) 46–53.
[7] K. de Haan, H. Ceylan Koydemir, Y. Rivenson, D. Tseng, E. Van Dyne, L. Bakic, D. Karinca, K. Liang, M. Ilango, E. Gumustekin, et al., Automated screening of sickle cells using a smartphone-based microscope and deep learning, npj Digit. Med. 3 (1) (2020) 1–9.
[8] C.I. Wilson, P.L. Hopkins, B. Cabello-Inchausti, S.J. Melnick, M.J. Robinson, The peripheral blood smear in patients with sickle cell trait: a morphologic observation, Lab. Med. 31 (8) (2000) 445–447.
[9] G. Dhaliwal, P.A. Cornett, L.M. Tierney Jr, Hemolytic anemia, Am. Fam. Phys. 69 (11) (2004) 2599–2606.
[10] G.S. Nowakowski, J.D. Hoyer, T.D. Shanafelt, C.S. Zent, T.G. Call, N.D. Bone, B. LaPlant, G.W. Dewald, R.C. Tschumper, D.F. Jelinek, et al., Percentage of smudge cells on routine blood smear predicts survival in chronic lymphocytic leukemia, J. Clin. Oncol. 27 (11) (2009) 1844.
[11] S.S. Patel, G.A. Aasen, M.M. Dolan, M.A. Linden, R.W. McKenna, V.K. Rudrapatna, B.J. Trottier, S.M. Drawz, Early diagnosis of intravascular large b-cell lymphoma: clues from routine blood smear morphologic findings, Lab. Med. 45 (3) (2014) 248–252.
[12] A.N. Khvastunova, S.A. Kuznetsova, L.S. Al-Radi, A.V. Vylegzhanina, A.O. Zakirova, O.S. Fedyanina, A.V. Filatov, I.A. Vorobjev, F. Ataullakhanov, Anti-cd antibody microarray for human leukocyte morphology examination allows analyzing rare cell populations and suggesting preliminary diagnosis in leukemia, Sci. Rep. 5 (1) (2015) 1–13.
[13] M. Sant, C. Allemani, C. Tereanu, R. De Angelis, R. Capocaccia, O. Visser, R. Marcos-Gragera, M. Maynadié, A. Simonetti, J.-M. Lutz, et al., Incidence of hematologic malignancies in Europe by morphologic subtype: results of the haemacare project, Blood 116 (19) (2010) 3724–3734.
[14] M. Doan, J.A. Sebastian, R.N. Pinto, C. McQuin, A. Goodman, O. Wolkenhauer, M.J. Parsons, J.P. Acker, P. Rees, H. Hennig, et al., Label-free assessment of red blood cell storage lesions by deep learning, BioRxiv (2018) 256180.
[15] A. Ojaghi, G. Carrazana, C. Caruso, A. Abbas, D.R. Myers, W.A. Lam, F.E. Robles, Label-free hematology analysis using deep-ultraviolet microscopy, Proc. Natl. Acad. Sci. 117 (26) (2020) 14779–14789.
[16] A. Ramoji, U. Neugebauer, T. Bocklitz, M. Foerster, M. Kiehntopf, M. Bauer, J. Popp, Toward a spectroscopic hemogram: Raman spectroscopic differentiation of the two most abundant leukocytes from peripheral blood, Anal. Chem. 84 (12) (2012) 5335–5342.
[17] C.G. Atkins, K. Buckley, M.W. Blades, R.F. Turner, Raman spectroscopy of blood and blood components, Appl. Spectrosc. 71 (5) (2017) 767–793.
[18] R.R. Jones, D.C. Hooper, L. Zhang, D. Wolverson, V.K. Valev, Raman techniques: fundamentals and frontiers, Nanoscale Res. Lett. 14 (1) (2019) 1–34.
[19] G.S. Verebes, M. Melchiorre, A. Garcia-Leis, C. Ferreri, C. Marzetti, A. Torreggiani, Hyperspectral enhanced dark field microscopy for imaging blood cells, J. Biophotonics 6 (11–12) (2013) 960–967.
[20] Q. Wang, J. Wang, M. Zhou, Q. Li, Y. Wang, Spectral-spatial feature-based neural network method for acute lymphoblastic leukemia cell identification via microscopic hyperspectral imaging technology, Biomed. Opt. Express 8 (6) (2017) 3017–3028.
[21] X. Liu, M. Zhou, S. Qiu, L. Sun, H. Liu, Q. Li, Y. Wang, Adaptive and automatic red blood cell counting method based on microscopic hyperspectral imaging technology, J. Opt. 19 (12) (2017) 124014.
[22] P.M.S. Roma, L. Siman, B. Hissa, U. Agero, E.M. Braga, O.N. Mesquita, Profiling of individual human red blood cells under osmotic stress using defocusing microscopy, J. Biomed. Opt. 21 (9) (2016) 090505.
[23] P. Roma, L. Siman, F. Amaral, U. Agero, O. Mesquita, Total three-dimensional imaging of phase objects using defocusing microscopy: application to red blood cells, Appl. Phys. Lett. 104 (25) (2014) 251107.
[24] V. Chhaniwal, A.S. Singh, R.A. Leitgeb, B. Javidi, A. Anand, Quantitative phase-contrast imaging with compact digital holographic microscope employing Lloyd's mirror, Opt. Lett. 37 (24) (2012) 5127–5129.
[25] S. Lee, H. Park, K. Kim, Y. Sohn, S. Jang, Y. Park, Refractive index tomograms and dynamic membrane fluctuations of red blood cells from patients with diabetes mellitus, Sci. Rep. 7 (1) (2017) 1–11.
[26] Y. Ozaki, H. Yamada, H. Kikuchi, A. Hirotsu, T. Murakami, T. Matsumoto, T. Kawabata, Y. Hiramatsu, K. Kamiya, T. Yamauchi, et al., Label-free classification of cells based on supervised machine learning of subcellular structures, PLoS ONE 14 (1) (2019) e0211347.
[27] G. Kim, D. Ahn, M. Kang, J. Park, D. Ryu, Y. Jo, J. Song, J.S. Ryu, G. Choi, H.J. Chung, et al., Rapid species identification of pathogenic bacteria from a minute quantity exploiting three-dimensional quantitative phase imaging and artificial neural network, Light: Sci. Appl. 11 (1) (2022) 1–12.
[28] D. Ryu, J. Kim, D. Lim, H.-S. Min, I.Y. Yoo, D. Cho, Y. Park, Label-Free White Blood Cell Classification Using Refractive Index Tomography and Deep Learning, BME Frontiers, 2021, p. 2021.
[29] G. Kim, Y. Jo, H. Cho, H.-s. Min, Y. Park, Learning-based screening of hematologic disorders using quantitative phase imaging of individual red blood cells, Biosens. Bioelectron. 123 (2019) 69–76.
[30] T. Go, J.H. Kim, H. Byeon, S.J. Lee, Machine learning-based in-line holographic sensing of unstained malaria-infected red blood cells, J. Biophotonics 11 (9) (2018) e201800101.
[31] J. Choi, H.-J. Kim, G. Sim, S. Lee, W.S. Park, J.H. Park, H.-Y. Kang, M. Lee, W. Do Heo, J. Choo, et al., Label-free three-dimensional analyses of live cells with deep-learning-based segmentation exploiting refractive index distributions, BioRxiv (2021).
[32] J. Lee, H. Kim, H. Cho, Y. Jo, Y. Song, D. Ahn, K. Lee, Y. Park, S.-J. Ye, Deep-learning-based label-free segmentation of cell nuclei in time-lapse refractive index tomograms, IEEE Access 7 (2019) 83449–83460.
[33] M. Lee, Y.-H. Lee, J. Song, G. Kim, Y. Jo, H. Min, C.H. Kim, Y. Park, Deep-learning-based three-dimensional label-free tracking and analysis of immunological synapses of car-t cells, eLife 9 (2020) e49023.
[34] Y. Jo, H. Cho, W.S. Park, G. Kim, D. Ryu, Y.S. Kim, M. Lee, H. Joo, H. Jo, S. Lee, et al., Data-driven multiplexed microtomography of endogenous subcellular dynamics, BioRxiv (2020).
[35] D. Ryu, D. Ryu, Y. Baek, H. Cho, G. Kim, Y.S. Kim, Y. Lee, Y. Kim, J.C. Ye, H.-S. Min, et al., Deepregularizer: rapid resolution enhancement of tomographic imaging using deep learning, IEEE Trans. Med. Imaging 40 (5) (2021) 1508–1518.
[36] Y. Rivenson, Y. Zhang, H. Günaydın, D. Teng, A. Ozcan, Phase recovery and holographic image reconstruction using deep learning in neural networks, Light: Sci. Appl. 7 (2) (2018) 17141.
[37] C.L. Chen, A. Mahjoubfar, L.-C. Tai, I.K. Blaby, A. Huang, K.R. Niazi, B. Jalali, Deep learning in label-free cell classification, Sci. Rep. 6 (1) (2016) 1–16.
[38] H. Hugonnet, M. Lee, Y. Park, Optimizing illumination in three-dimensional deconvolution microscopy for accurate refractive index tomography, Opt. Express 29 (5) (2021) 6293–6301.
[39] Z. Tian, C. Shen, H. Chen, T. He, Fcos: fully convolutional one-stage object detection, in: Proceedings of the IEEE/CVF International Conference on Computer Vision, 2019, pp. 9627–9636.

[40] Y. Liang, C. Pan, W. Sun, Q. Liu, Y. Du, Global context-aware cervical cell detection with soft scale anchor matching, Comput. Methods Programs Biomed. 204 (2021) 106061.
[41] M.M. Alam, M.T. Islam, Machine learning approach of automatic identification and counting of blood cells, Healthc. Technol. Lett. 6 (4) (2019) 103–108.
[42] J. Redmon, A. Farhadi, Yolov3: an incremental improvement, arXiv preprint, arXiv:1804.02767, 2018.
[43] K. Chen, J. Wang, J. Pang, Y. Cao, Y. Xiong, X. Li, S. Sun, W. Feng, Z. Liu, J. Xu, Z. Zhang, D. Cheng, C. Zhu, T. Cheng, Q. Zhao, B. Li, X. Lu, R. Zhu, Y. Wu, J. Dai, J. Wang, J. Shi, W. Ouyang, C.C. Loy, D. Lin, MMDetection: open mmlab detection toolbox and benchmark, arXiv preprint, arXiv:1906.07155, 2019.
[44] K. He, X. Zhang, S. Ren, J. Sun, Deep residual learning for image recognition, in: Proceedings of the IEEE Conference on Computer Vision and Pattern Recognition, 2016, pp. 770–778.
[45] Z. Liu, Y. Lin, Y. Cao, H. Hu, Y. Wei, Z. Zhang, S. Lin, B. Guo, Swin transformer: hierarchical vision transformer using shifted windows, in: Proceedings of the IEEE/CVF International Conference on Computer Vision, 2021, pp. 10012–10022.
[46] A. Vaswani, N. Shazeer, N. Parmar, J. Uszkoreit, L. Jones, A.N. Gomez, Ł. Kaiser, I. Polosukhin, Attention is all you need, Adv. Neural Inf. Process. Syst. 30 (2017).
[47] R. Barer, Interference microscopy and mass determination, Nature 169 (4296) (1952) 366–367.
[48] G. Popescu, Y. Park, N. Lue, C. Best-Popescu, L. Deflores, R.R. Dasari, M.S. Feld, K. Badizadegan, Optical imaging of cell mass and growth dynamics, Am. J. Physiol., Cell Physiol. 295 (2) (2008) C538–C544.
[49] O. Zhernovaya, O. Sydoruk, V. Tuchin, A. Douplik, The refractive index of human hemoglobin in the visible range, Phys. Med. Biol. 56 (13) (2011) 4013.
[50] Y. Sung, A. Tzur, S. Oh, W. Choi, V. Li, R.R. Dasari, Z. Yaqoob, M.W. Kirschner, Size homeostasis in adherent cells studied by synthetic phase microscopy, Proc. Natl. Acad. Sci. 110 (41) (2013) 16687–16692.
[51] A. Mashaghi, M. Swann, J. Popplewell, M. Textor, E. Reimhult, Optical anisotropy of supported lipid structures probed by waveguide spectroscopy and its application to study of supported lipid bilayer formation kinetics, Anal. Chem. 80 (10) (2008) 3666–3676.
[52] L. Van der Maaten, G. Hinton, Visualizing data using t-sne, J. Mach. Learn. Res. 9 (11) (2008).